Dalton Transactions

ROYAL SOCIETY OF CHEMISTRY

COMMUNICATION

View Article Online
View Journal | View Issue



Cite this: *Dalton Trans.*, 2026, **55**, 3672

Received 16th January 2026,
Accepted 9th February 2026

DOI: 10.1039/d6dt00112b

rsc.li/dalton



# Synthetic method analysis of $Ir_{0.85}Bi_{0.15}$ solid-solution nanoparticles with excellent hydrazine-decomposition activity

Xinling Xiong,[a,b] Zhenduo Liu[c] and Bo Huang *[a,b,d,e]

**Atomic-level homogeneously mixed and well-dispersed $Ir_{0.85}Bi_{0.15}$ solid-solution nanoparticles (NPs) were synthesized successfully for the first time despite large differences of crystal structures, redox potentials and atomic radii between Ir and Bi. Compared with Ir, the $Ir_{0.85}Bi_{0.15}$ solid-solution NPs exhibited superior cost-efficiency in hydrazine decomposition.**

Precious metal-based catalysts, particularly those involving platinum-group metals (PGMs), have been extensively investigated for applications in diverse important fields, such as the automotive sector,[1,2] drug delivery,[3,4] fuel cells[5,6] and aerospace.[7,8] However, their high cost and limited natural abundance have motivated continuous efforts to enhance both the catalytic activity and utilization efficiency of PGMs. Recently, various atomically dispersed alloy structures including single-atom alloys,[9] intermetallic compounds[10] and solid solutions,[11,12] have attracted considerable attention. Among those, solid-solution alloys formed between PGMs and nonprecious elements, with random atomic-level mixing, largely controllable ratios and greatly modified electronic states, have demonstrated significant potential for improving their intrinsic performances.[13,14] Nevertheless, synthesizing homogeneous PGM/nonprecious solid-solution nanoparticles (NPs) remains challenging due to their inherent thermodynamic instability under equilibrium conditions.

As a PGM, iridium (Ir) demonstrates excellent activities in several pivotal catalytic reactions, including hydrogen evolution reaction,[15] oxygen evolution reaction[16] and hydrazine ($N_2H_4$) decomposition.[17,18] Despite its remarkable performance, the high cost and rareness of Ir necessitate improving its catalytic performances and reducing its usage. Thus, solid-solution alloying of Ir with nonprecious metals could be a competitive choice. Owing to its natural abundance and low cost, bismuth (Bi) is regarded as an ideal candidate for partially substituting Ir. However, due to the large differences of crystal structures,[19,20] redox potentials[21] and atomic radii[22] between Ir and Bi, there are great challenges in synthesizing Ir–Bi solid solutions. Given that Bi possesses a relatively larger atomic radius compared to Ir, their alloys tend to form thermodynamically stable intermetallic compound phases[23–25] rather than solid-solution phases. Moreover, no Ir–Bi solid-solution NPs have been reported to date.

In this study, we have synthesized face-centred cubic (fcc)-structure $Ir_{0.85}Bi_{0.15}$ solid-solution NPs mixed homogeneously for the first time. The effects of the precursor, reducing agents and protecting agents on the formation of Ir–Bi solid-solution NPs were also analysed. Furthermore, the as-synthesized $Ir_{0.85}Bi_{0.15}$ solid-solution NPs showed much higher hydrazine decomposition activity than pure Ir NPs.

The polyol method was employed to synthesize homogeneously mixed Ir–Bi solid-solution NPs. Considering the previous synthesis of $Pt_2Bi$ NPs,[26] diethylene glycol (DEG) served as both the solvent and reducing agent. $IrCl_3{\cdot}3H_2O$ and $BiCl_3$ were chosen as the precursors with the same ligand. 49.4 mg (0.14 mmol) $IrCl_3{\cdot}3H_2O$ and 18.9 mg (0.06 mmol) $BiCl_3$ in 20 mL DEG were added dropwise for 5 min into a mixture solution of 80 mL DEG and 66 mg (0.6 mmol) polyvinylpyrrolidone (PVP) at 190 °C under magnetic stirring. The reaction mixture was kept for 5 min, and then cooled to room temperature. After the reaction, the black solution was centrifuged, washed with ethyl acetate, acetone, ethanol and petroleum ether three times, and dried under vacuum. The black powder was collected and denoted as sample 1.

To investigate the crystal structure of the as-synthesized Ir–Bi alloy, X-ray powder diffraction (XRPD) measurements

[a]*School of Chemical Engineering and Technology, Xi'an Jiaotong University, Innovation Harbour, Xi-xian New District, Xi'an 712000, China. E-mail: bohuang@xjtu.edu.cn*
[b]*National Innovation Platform (Center) for Industry-Education Integration of Energy Storage Technology, Xi'an Jiaotong University, Innovation Harbour, Xi-xian New District, Xi'an 712000, China*
[c]*Xi'an Aerospace Propulsion Institute, Aerospace Propulsion Technology Research Institute, Feitian Road, Aerospace District, Xi'an 710100, China*
[d]*School of Future Technology, Xi'an Jiaotong University, Innovation Harbour, Xi-xian New District, Xi'an 712000, China*
[e]*Shaanxi Tianyi Element Technology Co., Ltd, High-Tech Industrial Development Zone, Xianyang 712000, China*

were conducted. The XRPD pattern of sample 1 showed the same fcc structure as that of fcc-Ir NPs (Fig. 1a). As shown in Fig. 1a, the Rietveld refinement on the XRPD pattern of sample 1 estimated the lattice constant as 3.854(1) Å, larger than that of fcc-Ir NPs at 3.839(7) Å (Fig. S1), which showed the possible formation of Ir–Bi solid solution. To clarify the dispersion and mixing states of the as-synthesized Ir–Bi alloy, high-angle annular dark-field scanning transmission electron microscopy (HAADF-STEM) and STEM-energy-dispersive X-ray (EDX) mapping measurements were performed. The mean diameter of sample 1 from the HAADF-STEM image was 2.7 ± 0.4 nm (Fig. S2). The STEM-EDX maps (Fig. 1b) show that most Bi and Ir dispersed homogeneously as a Ir–Bi alloy, while some Bi still grew on the outside of alloy NPs, due to the different reaction times between the precursors of Bi and Ir (Fig. S3). Additionally, X-ray Fluorescence (XRF) measurement of sample 1 revealed that the ratio of Ir and Bi was 0.91 : 0.09, being only one third of the Bi nominal ratio, maybe due to the preferred reduction of the Ir precursor than the Bi precursor during the 5 min reaction (Fig. S3).

For coreduction of Ir and Bi elements, ethylene glycol (EG) with a stronger reducing ability was used to synthesize sample 2 (see more details in the SI). For characterization, XRPD, TEM, HAADF-STEM, STEM-EDX mapping and XRF measurements were conducted (Fig. S4 and S5). The Rietveld refinement on the XRPD pattern of sample 2 showed an fcc structure, with a lattice constant of 3.853(3) Å (Fig. S4a), similar to that of sample 1. The TEM image (Fig. S5) shows that sample 2 had the mean diameter of 2.8 ± 0.5 nm, but agglomerated. This might come from the tendency to agglomerate with too much reduced Bi atoms[23] under the strong reducing ability of EG. The STEM-EDX mapping measurement of sample 2 revealed that the mixing state of Ir and Bi was improved significantly, and its Ir : Bi atomic ratio was 0.91 : 0.09 (Fig. S4b), which was consistent with XRF measurement results. The EG with a strong reducing ability reduced more Ir and Bi atoms, and they tended to co-nucleate and grow due to the lower viscosity of EG than that of DEG.[27]

To increase the ratio of Bi in the alloy, $Bi(NO_3)_3{\cdot}5H_2O$ was used instead of $BiCl_3$ together with $IrCl_3{\cdot}3H_2O$ to synthesize sample 3 (see more details in the SI). The lattice constant of sample 3 from Rietveld refinement was 3.885(3) Å (Fig. 2a), larger than that of sample 2 (3.853 Å). The TEM image indicated that the mean diameter of sample 3 was 1.5 ± 0.2 nm, smaller than that of sample 2, but still agglomerated (Fig. S6). To figure out the reason for the smaller size, the reaction time difference between $Bi(NO_3)_3{\cdot}5H_2O$ and $BiCl_3$ should be considered. Since the steric hindrance of $Bi(NO_3)_3{\cdot}5H_2O$ is larger than that of $BiCl_3$,[28] the reaction time of $Bi(NO_3)_3{\cdot}5H_2O$ was longer, thereby decreasing the concentration of reduced Bi atoms (Fig. S7). Generally, Ir NPs have small size, while Bi NPs possess large size, indicating that Ir has a relatively fast nucleation rate, while Bi has a rapid growth rate. Hence, the decreased Bi concentration favored the nucleation process rather than the growth process, leading to a decrease of size. Moreover, the STEM-EDX measurement indicated the homogeneous mixing of Ir and Bi with a ratio of 0.85 : 0.15 for sample 3 (Fig. 2b), improved from sample 2. This improvement in the Bi ratio is attributed to the etching effect. Generally, protons and anions from strong acids in solution could etch the NPs consisting of metals with low redox potentials.[21] Although both $Cl^-$ and $NO_3^-$ are strong acid anions, $Bi(NO_3)_3{\cdot}5H_2O$ with bidentate coordination from $NO_3^-$ might release less $NO_3^-$ than the monodentate-coordinated $BiCl_3$.[28] The lower anion concentration of sample 3 resulted in weaker etching, and achieved a higher Bi ratio than that of sample 2.

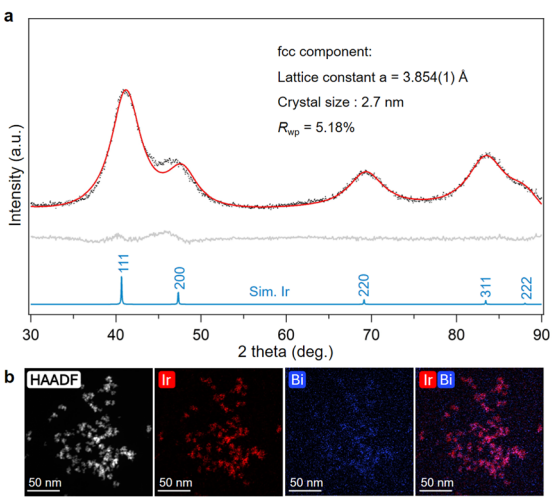


**Fig. 1** (a) Rietveld refinement on the XRPD pattern of sample 1; the black dots and red, grey and blue curves represent raw data, calculated patterns, different profiles and simulated Ir at 300 K. The radiation wavelength was 1.54056 Å. (b) HAADF-STEM image and STEM-EDX maps of Ir-M (red), Bi-M (blue) and an overlay in sample 1.

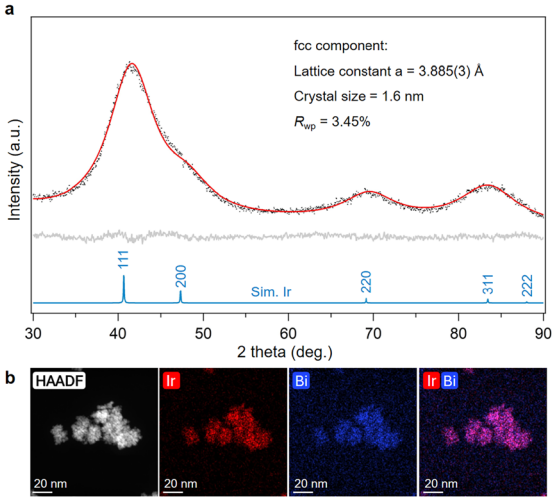


**Fig. 2** (a) Rietveld refinement on the XRPD pattern of sample 3; the black dots and red, grey and blue curves represent raw data, calculated patterns, different profiles and simulated Ir at 300 K. The radiation wavelength was 1.54056 Å. (b) HAADF-STEM image and STEM-EDX maps of Ir-M (red), Bi-M (blue) and an overlay in sample 3.

The amount of PVP was increased in sample 4 to solve the problem of agglomeration in sample 3 (detailed in Table S1), and the HAADF-STEM image revealed the much-improved dispersion (Fig. S8). As a protecting agent, more PVP effectively wrapped the Ir–Bi NPs, inhibiting their collision and agglomeration (Fig. 3a). The Ir–Bi NPs of sample 4 presented an fcc structure as determined from the Rietveld refinement, with a lattice constant of 3.880(2) Å (Fig. S9). STEM-EDX mapping measurement exhibited that Ir mixed homogeneously with Bi and the atomic ratio of Bi in sample 4 was nearly 15.0% (Fig. 3b), which strongly demonstrated the successful synthesis of $Ir_{0.85}Bi_{0.15}$ solid-solution NPs. Moreover, the same method was used to synthesize other ratio Ir–Bi solid-solution NPs, as sample 5. The Ir–Bi NPs of sample 5 also presented the fcc structure (Fig. S10a) and homogeneous element distribution (Fig. S10b), with a mean diameter of 2.3 nm (Fig. S11) and a Bi content of 7.2 at%. The lattice constants calculated by Rietveld refinement were linear to Bi contents following Vegard's law (Fig. S9, S10a and S12), providing strong evidence for the formation of $Ir_{1-x}Bi_x$ solid solutions. Furthermore, high-resolution (HR)-TEM characterization confirmed the highly crystalline identity of fcc-$Ir_{0.85}Bi_{0.15}$ solid-solution NPs (Fig. 3c). The measured distances of fcc-$Ir_{0.85}Bi_{0.15}$ {111} and {002} planes were 0.225 and 0.195 nm, respectively, consistent with the calculated values from Rietveld refinement (2.253 Å and 1.952 Å), which further demonstrated the formation of fcc-$Ir_{0.85}Bi_{0.15}$ solid-solution NPs.

To date, Ir is the most active for $N_2H_4$ decomposition among all the elements.[17,18] With the formation of Ir–Bi solid-solution NPs, the decomposition activity of $N_2H_4$ may be higher than that of pure Ir. Therefore, the Ir, Bi, Ir–Bi physical mixture, $Ir_{0.93}Bi_{0.07}$ and $Ir_{0.85}Bi_{0.15}$ solid-solution NPs were loaded on γ-$Al_2O_3$, and their performances in $N_2H_4$ decomposition were investigated (see more experimental details in the SI).

The $N_2H_4$ decomposition activity for the five catalysts at room temperature was evaluated from the generated $N_2$ and $H_2$ volumes over time. After normalization by masses of Ir and Bi metals, $Ir_{0.85}Bi_{0.15}$ exhibited the fastest gas generation rate of about 9102.4 mmol $g_{metal}^{-1}$ $h^{-1}$, which was 1.4 times that of Ir (6577.9 mmol $g_{Ir}^{-1}$ $h^{-1}$), while the Bi showed no activity for $N_2H_4$ decomposition (Fig. 4a). As Ir is a precious metal while Bi is an abundant metal, the gas generation rate based on the Ir mass of $Ir_{0.85}Bi_{0.15}$ was 10 993.2 mmol $g_{Ir}^{-1}$ $h^{-1}$, which was 1.7 times that of Ir (6577.9 mmol $g_{Ir}^{-1}$ $h^{-1}$). This indicated that $Ir_{0.85}Bi_{0.15}$ had a much better intrinsic $N_2H_4$ decomposition activity than Ir. Moreover, $Ir_{0.85}Bi_{0.15}$ demonstrated good cycling stability, maintaining its initial activity after 6 cycles (Fig. 4b) and 97% retention of its initial activity after 3 h (Fig. S13), suggesting its good stability. The slight increase in catalytic activity between 10 and 40 minutes (Fig. 4b) may be primarily attributed to the exothermic nature of the $N_2H_4$ decomposition reaction. Moreover, the reaction intermediates, particularly $NH_x$* species, might poison the catalytically active sites to decrease the activity over time.[29] The post-reaction $Ir_{0.85}Bi_{0.15}$ was characterized by STEM-EDX measurement (Fig. S14), which confirmed nearly no aggregation during the reaction process. From the STEM-EDX mapping measurement, the Ir/Bi ratio of the post-reaction $Ir_{0.85}Bi_{0.15}$ was estimated to be 85.7/14.3, consistent with that of the original catalyst before reaction, which suggested nearly no loss of Bi during the reaction process.

To investigate the electronic states of $Ir_{0.85}Bi_{0.15}$ solid solution, X-ray photoelectron spectroscopic (XPS) measurements were carried out for the $Ir_{0.85}Bi_{0.15}$ solid-solution NPs with Ir and Bi NP references. The $Ir^0$ 4f peaks of $Ir_{0.85}Bi_{0.15}$ shifted to lower energy compared to those of Ir NPs, while the $Bi^0$ 4f

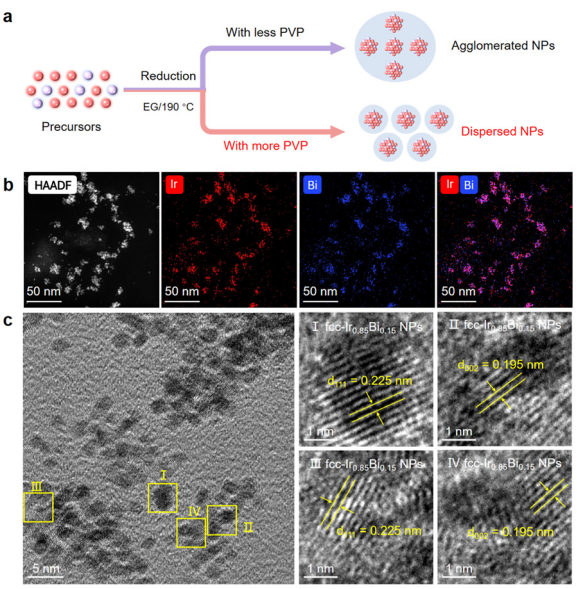


**Fig. 3** (a) Schematic illustration of the effect of PVP during the nanoparticle's formation. (b) HAADF-STEM image and STEM-EDX maps of Ir-M (red), Bi-M (blue) and an overlay in sample 4. (c) HR-TEM images of sample 4.

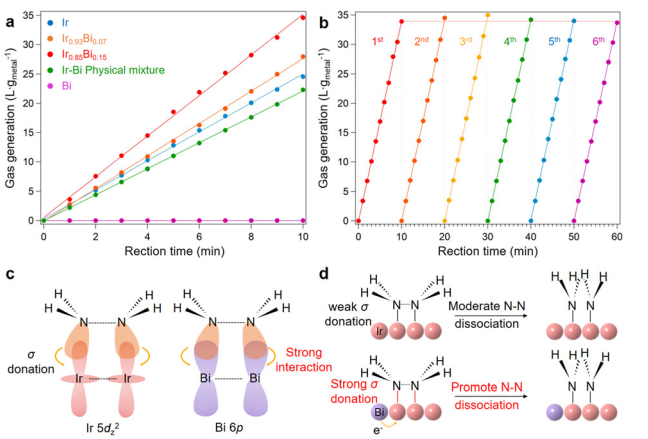


**Fig. 4** (a) The time-dependent $N_2$ and $H_2$ generation curves for $N_2H_4$ decomposition at room temperature. (b) The volumes of $N_2$ and $H_2$ generated from the $N_2H_4$ decomposition of $Ir_{0.85}Bi_{0.15}$ for 6 cycles. (c) σ donations from N-lone pairs in $N_2H_4$ to Ir-$d_{z^2}$ in $Ir_{0.85}Bi_{0.15}$ and strong interaction between Bi 6p and N 2p orbitals. (d) Comparison on the N–N dissociation processes of Ir and $Ir_{0.85}Bi_{0.15}$.

peaks of $Ir_{0.85}Bi_{0.15}$ shifted to higher energy compared to those of Bi NPs, proving the electron transfer from Bi to Ir in $Ir_{0.85}Bi_{0.15}$ (Fig. S15 and Table S2). In general, the rate determining step for Ir in $N_2H_4$ decomposition is considered to be N–N dissociation in $H_2N$–$NH_2$.[18] On the one hand, the strong interaction between the Bi 6p orbitals and N 2p orbitals[30,31] may enable Bi to act as a greater acceptor of σ donation from $N_2H_4$, owing to its greater spatial overlap coming from the larger atomic radius of Bi and more efficient p–p interaction rather than d–p interaction (Fig. 4c). This may enhance electron acceptance, promoting the dissociation of the rate-determining N–N bonds and thereby improving the decomposition of $N_2H_4$ (Fig. 4c). On the other hand, the electrons transferred from Bi to $Ir_{0.85}Bi_{0.15}$-Ir site improved the electron density in the Ir d-band, which strengthened the σ donation between the Ir $d_{z^2}$ orbital and N-lone pairs in $N_2H_4$ or its intermediates. This could weaken the N–N bond, thereby promoting the rate-determining N–N bond dissociation, and accelerate the overall decomposition process (Fig. 4d). Hence, the outstanding catalytic activity of $Ir_{0.85}Bi_{0.15}$ solid-solution NPs may be attributed to the synergetic effect between Ir and Bi, where Ir sites selectively activate N–H bond dissociation,[32] while adjacent Bi sites effectively promote the N–N bond dissociation, thereby cooperatively enhancing the overall decomposition process.

In summary, we have synthesized $Ir_{0.85}Bi_{0.15}$ solid-solution NPs for the first time by a coreduction method, overcoming great challenges from the large differences of crystal structures, redox potentials and atomic radii between Ir and Bi. The XRPD Rietveld refinement and TEM and STEM-EDX mapping measurements confirmed the formation of fcc-$Ir_{0.85}Bi_{0.15}$ solid-solution NPs with homogeneous distributions of Ir and Bi. Additionally, the investigation of Ir–Bi solid-solution NP syntheses has proved the significant effects of the precursor- and reducing and protecting agents on the NP formation. Moreover, the $Ir_{0.85}Bi_{0.15}$ solid-solution NPs demonstrated excellent intrinsic activity for $N_2H_4$ decomposition than Ir.

## Author contributions

Xinling Xiong: investigation, data curation, data analysis, and writing of the original draft. Zhenduo Liu: investigation and data curation. Bo Huang: investigation, writing – review and editing, and supervision. All authors have given approval to the final version of the manuscript.

## Conflicts of interest

There are no conflicts to declare.

## Data availability

The data that support the findings of this study are available in the supplementary information (SI) of this article. Supplementary information: additional data from experimental details, XRPD patterns, Rietveld refinements, XPS analysis, TEM images, HAADF-STEM images, and STEM-EDX maps of our samples. See DOI: https://doi.org/10.1039/d6dt00112b.

## Acknowledgements

This research was supported by the National Innovation Platform (Center) for Industry-Education Integration of Energy Storage Technology of Xi'an Jiaotong University, Fundamental Research Fund of Xi'an Jiaotong University, xzd012023049, Young Talents Foundation of Shaanxi Province and Scientists & Engineers Innovation Team Foundation of Shaanxi Province (program no. 2023KXJ-156), Technology Innovation Leading Program of Shaanxi (program no. 2023QYPY-18), and Shanghai Pujiang Program (program no. 23PJD002). We also thank Dr Chao Li at the Instrument Analysis Centre of Xi'an Jiaotong University for STEM-EDX characterization instructions.

## References

1 M. Chhetri, M. Wan, Z. Jin, J. Yeager, C. Sandor, C. Rapp, H. Wang, S. Lee, C. J. Bodenschatz, M. J. Zachman, F. Che and M. Yang, *Nat. Commun.*, 2023, **14**, 3075.
2 Z. Tan and B. Huang, *Angew. Chem., Int. Ed.*, 2024, **63**, e202400496.
3 F. Peng, D. Wang, Y. Tian, H. Cao, Y. Qiao and X. Liu, *Sci. Rep.*, 2017, **7**, 8167.
4 W. Choi and D. S. Kohane, *ACS Nano*, 2024, **18**, 22780–22792.
5 H. Su and Y. Hu, *Ind. Eng. Chem. Res.*, 2024, **63**, 4390–4396.
6 C. Cui, L. Gan, H. Li, S. Yu, M. Heggen and P. Strasser, *Nano Lett.*, 2012, **12**, 5885–5889.
7 X. Liu, C. Liu, M. Chen, C. Bai, X. Zhang and L. Wei, *ACS Appl. Nano Mater.*, 2024, **7**, 16609–16619.
8 J. G. Hoekstra, S. B. Qadri, J. R. Scully and J. M. Fitz-Gerald, *Adv. Eng. Mater.*, 2005, **7**, 805–809.
9 R. J. Bunting, F. Wodaczek, T. Torabi and B. Cheng, *J. Am. Chem. Soc.*, 2023, **145**, 14894–14902.
10 H. Itahara, Y. Takatani, N. Takahashi and S. Kosaka, *Inorg. Chem.*, 2020, **59**, 13583–13588.
11 X. Sun, Y. He, M. Wang, Q. Cheng, Y. Huan, S. Liu, J. Liu, T. Qian, C. Yan and J. Lu, *ACS Nano*, 2025, **19**, 8189–8199.
12 J. Gao and B. Huang, *Adv. Sci.*, 2025, **12**, 2504161.
13 Z. Tan, M. Haneda, H. Kitagawa and B. Huang, *Angew. Chem., Int. Ed.*, 2022, **61**, e202202588.
14 Y. Liu, W. Zhai, P. Cui, L. Li, Z. Dai and B. Huang, *Chem. Mater.*, 2024, **36**, 8965–8975.
15 S. E. Jun, Y.-H. Kim, J. Kim, W. S. Cheon, S. Choi, J. Yang, H. Park, H. Lee, S. H. Park, K. C. Kwon, J. Moon, S.-H. Kim and H. W. Jang, *Nat. Commun.*, 2023, **14**, 609.

16 C. Hu, K. Yue, J. Han, X. Liu, L. Liu, Q. Liu, Q. Kong, C.-W. Pao, Z. Hu, K. Suenaga, D. Su, Q. Zhang, X. Wang, Y. Tan and X. Huang, *Sci. Adv.*, 2023, **9**, eadf9144.
17 T. S. Neto, F. Dias, A. Cobo and G. Cruz, *Chem. Eng. J.*, 2011, **173**, 220–225.
18 X. Lu, S. Francis, D. Motta, N. Dimitratos and A. Roldan, *Phys. Chem. Chem. Phys.*, 2020, **22**, 3883–3896.
19 D. G. Pettifor, *J. Phys. C: Solid State Phys.*, 1970, **3**, 367.
20 P. Hofmann, *Prog. Surf. Sci.*, 2006, **81**, 191–245.
21 P. Vanýsek, in *CRC Handbook of Chemistry and Physics*, ed. D. R. Lide, CRC Press, Boca Raton, Florida, 84th edn, 2005.
22 M. Rahm, R. Hoffmann and N. W. Ashcroft, *Chem. – Eur. J.*, 2016, **22**, 14625.
23 R. Boldt, A. Grigas, M. Heise, T. Herrmannsdörfer, A. Isaeva, S. Kaskel, D. Köhler, M. Ruck, R. Skrotzki and J. Wosnitza, *Z. Anorg. Allg. Chem.*, 2012, **638**, 2035–2043.
24 M. Heise, B. Rasche, A. Isaeva, A. I. Baranov, M. Ruck, K. Schäfer, R. Pöttgen, J.-P. Eufinger and J. Janek, *Angew. Chem., Int. Ed.*, 2014, **53**, 7344–7348.
25 A. Isaeva, M. Ruck, K. Schäfer, U. C. Rodewald and R. Pöttgen, *Inorg. Chem.*, 2015, **54**, 885–889.
26 X. Wang, M. Xie, F. Lyu, Y. Yiu, Z. Wang, J. Chen, L. Chang, Y. Xia, Q. Zhong, M. Chu, H. Yang, T. Cheng, T. Sham and Q. Zhang, *Nano Lett.*, 2020, **20**, 7751–7759.
27 B. Huang, H. Kobayashi, T. Yamamoto, S. Matsumura, Y. Nishida, K. Sato, K. Nagaoka, M. Haneda, S. Kawaguchi, Y. Kubptak and H. Kitagawa, *Chem. Sci.*, 2020, **11**, 11413.
28 M. P. Herpin and K. Sudarsanam, *Bull. Soc. Fr. Mineral. Cristallogr.*, 1965, **88**, 590–694.
29 J. Gao, J. Zheng, H. Deng, Z. Tan, J. Zhao and B. Huang, *ACS Nano*, 2026, **20**, 2545–2555.
30 Y. Wan, H. Zhou, M. Zheng, Z. Huang, F. Kang, J. Li and R. Lv, *Adv. Funct. Mater.*, 2021, **31**, 2100300.
31 Y. Hao, Y. Guo, L. Chen, M. Shu, X. Wang, T. Bu, W. Gao, N. Zhang, X. Su, X. Feng, J. Zhou, B. Wang, C. Hu, A. Yin, R. Si, Y. Zhang and C. Yan, *Nat. Catal.*, 2019, **2**, 448–456.
32 Z. Huang, J. Zhou and J. F. Hartwig, *J. Am. Chem. Soc.*, 2010, **132**, 11458–11460.